






## Tunable magnetic structures in the helimagnet $\text{YBa}(\text{Cu}_{1-x}\text{Fe}_x)_2\text{O}_5$

Chun-Hao Lai <sup>1</sup>, Chin-Wei Wang <sup>2</sup>, Hung-Cheng Wu,<sup>3</sup> Yu-Hui Liang <sup>1</sup>, Andrew J. Studer,<sup>4</sup>  
Wei-Tin Chen <sup>5,6,\*</sup> and Chao-Hung Du <sup>1,†</sup>

<sup>1</sup>Department of Physics, Tamkang University, Tamsui 251301, Taiwan

<sup>2</sup>National Synchrotron Radiation Research, Hsinchu 300092, Taiwan

<sup>3</sup>Institute of Multidisciplinary Research for Advanced Materials, Tohoku University, Sendai 980–8577, Japan

<sup>4</sup>Australian Nuclear Science and Technology Organization, NSW 2234, Australia

<sup>5</sup>Center for Condensed Matter Sciences and Center of Atomic Initiative for New Materials,  
National Taiwan University, Taipei 106319, Taiwan

<sup>6</sup>Taiwan Consortium of Emergent Crystalline Material,

National Science and Technology Council, Taipei 106214, Taiwan



(Received 30 October 2023; accepted 12 April 2024; published 7 May 2024)

We report the tunable magnetic structures in the helimagnet  $\text{YBa}(\text{Cu}_{1-x}\text{Fe}_x)_2\text{O}_5$  by changing various Cu/Fe ratios. The magnetic properties and structures of the samples were studied by using neutron- and x-ray powder diffraction and susceptibility measurements. The parent material  $\text{YBaCuFeO}_5$  (YBCFO) exhibits two antiferromagnetic (AFM) transitions at  $T_{N1} \sim 450$  K and  $T_{N2} \sim 175$  K. At  $T_{N1}$ , YBCFO shows a commensurate (CM) spin ordering with a  $q$ -wave vector  $\mathbf{k}_{c1} = (1/2 \ 1/2 \ 1/2)$ , which transfers to a spiral magnetic ordering at  $T_{N2}$  with an incommensurate  $q$ -wave vector  $(1/2 \ 1/2 \ 1/2 \pm \delta)$ ,  $\delta$  being the incommensurability. Using neutron powder diffraction for samples with  $0.490 \leq x \leq 0.505$ ,  $T_{N2}$  was observed to systematically increase from 125 to 236 K as a function of the Cu/Fe ratio. For  $x = 0.510$  and  $0.515$ , additional magnetic reflections with a propagation vector  $\mathbf{k}_{c2} = (1/2 \ 1/2 \ 0)$  appear below  $T_{N3} \sim 245$  and  $269$  K, respectively. This CM phase shows a collinear magnetic ordering. These transition temperatures are consistent with the AFM transitions of the magnetization data. Experiments were also conducted to synthesize the samples with different thermal treatments, demonstrating the  $T_{N2}$  and  $T_{N3}$  to be sensitive to the annealing conditions. These results can be understood within the framework of the random distributions of the dopants (impurities) at the  $B$  site of a double-perovskite lattice and demonstrate that the magnetic ordering in the helimagnet YBCFO can be systematically tuned by changing the Cu/Fe ratio.

DOI: [10.1103/PhysRevMaterials.8.054404](https://doi.org/10.1103/PhysRevMaterials.8.054404)

### I. INTRODUCTION

In the continuing research for multiferroic materials, a double perovskite,  $\text{YBaCuFeO}_5$  (YBCFO), has attracted a great deal of attention because it has been reported to be a good candidate showing the type II multiferroic property with a high transition temperature of around 230 K [1]. Unlike type I multiferroics, whose ferroelectricity and ferromagnetism (or antiferromagnetism) come from dissimilar microscopic sources, the ferroelectric polarization of type II multiferroics is induced by the specific magnetic ordering [2,3], which means the multiferroicity is no longer a privilege for particular crystalline point groups [3]. Most important, this mechanism allows extreme magnetoelectric coupling. However, type II multiferroic materials are novel and their transition temperatures are usually low, since the ferroelectricity has the same transition temperature as the magnetism, so raising the transition temperatures of the multiferroic materials has become a hot topic, and YBCFO seems to be a promising candidate.

$A$ -site or  $B$ -site substitution has been proven as an efficient approach to tuning the physical properties of perovskite oxides [4–6]. For example, substituting Sr for the  $A$  site of  $\text{LaMnO}_3$  can alter the ratio of  $\text{Mn}^{3+}$  and  $\text{Mn}^{4+}$ , which brings different extent of double-exchange interaction that turns  $\text{La}_{1-x}\text{Sr}_x\text{MnO}_3$  from an insulator into a metal phase [4]. Meanwhile, substituting Ni for the  $B$  site of  $\text{Sr}_2\text{FeMoO}_6$  can improve the long-range ordering of  $B$  sites and enhance the ferrimagnetism of  $\text{Sr}_2(\text{Fe}_{1-x}\text{Ni}_x)\text{MoO}_6$  [5].  $B$ -site ordering of perovskite oxides can also benefit from  $A$ -site doping; as proved by Bai *et al.*, the hybridization of the Bi  $6s$  and the O  $2p$  orbitals can stabilize the  $B$ -site ordering of  $\text{La}_{2-x}\text{Bi}_x\text{CoMnO}_6$  [6]. Overall, the diversity and ordering of the  $B$  sites are critical to the material research of perovskite oxides.

As for  $\text{YBaCuFeO}_5$ , Shang *et al.* have investigated how Sr doping and rare-earth  $A$ -site substitution affect the commensurate–incommensurate (CM-ICM) phase transition of YBCFO [7], succeeded by Mn-doped YBCFO with a new magnetic ordering revealed by Zhang *et al.* [8]. On the other hand, Morin *et al.* calculated the stability of several YBCFO supercells with distinct Cu/Fe distribution [9] and demonstrated the effect of  $B$ -site ordering on the antiferromagnetic

\*weitinchen@ntu.edu.tw

†chd@mail.tku.edu.tw

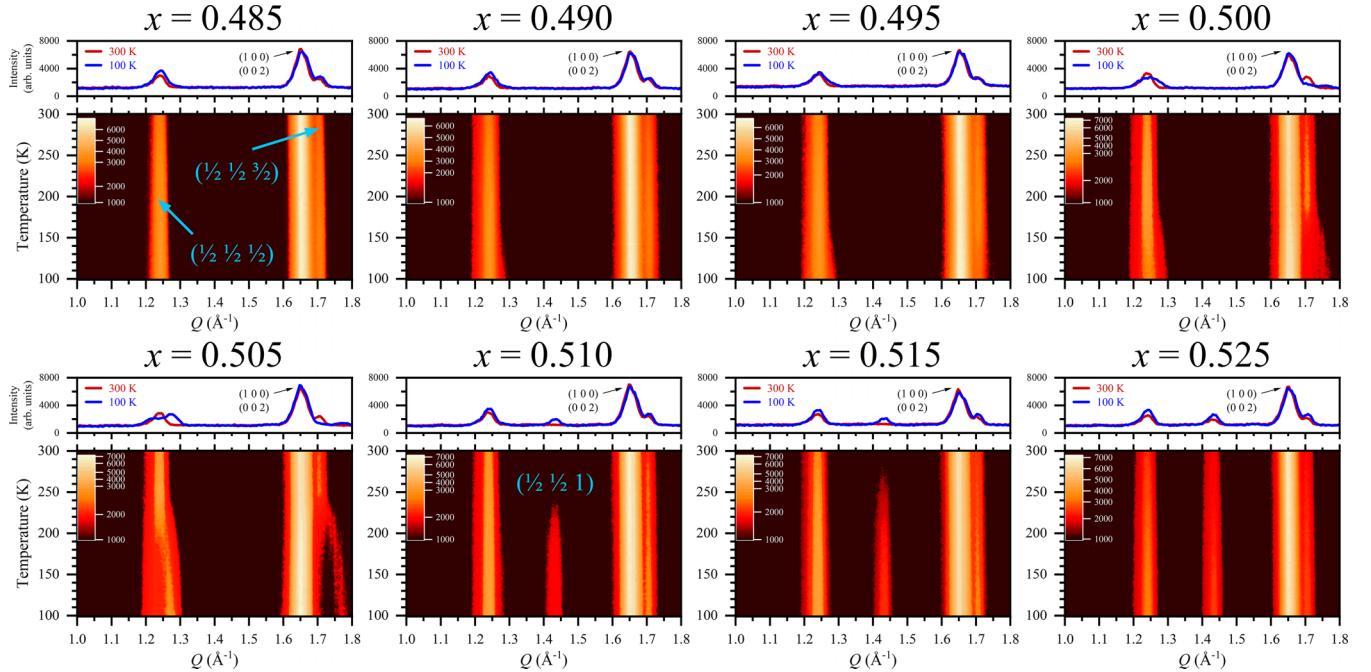


FIG. 1. Two-dimensional (2D) contours of eight  $\text{YBa}(\text{Cu}_{1-x}\text{Fe}_x)_2\text{O}_5$  samples with distinct Cu/Fe ratios illustrate the temperature dependence of NPD patterns measured from 100 to 300 K, and the two patterns on the edges of this temperature range are displayed above each contour. These figures focus on the low- $Q$  region because the magnetic reflections decay intensely with a larger  $Q$  value [19]. Magnetic reflections  $(1/2\ 1/2\ 1/2)$ ,  $(1/2\ 1/2\ 3/2)$ , and  $(1/2\ 1/2\ 1)$  are pointed out on the contour that they first revealed. Notice the resolution of Wombat is not capable of separating two ICM satellites from the CM peaks, so the CM peaks seem to broaden after phase transition, but for  $x = 0.505$ , satellites are clearer than other samples since it has the highest  $T_{N2}$  of the CM-ICM transition, while the incommensurability  $\delta$  is getting larger upon cooling down from  $T_{N2}$ .

(AFM) transition temperatures by varying the cooling rate of the synthesis process [10]. By developing a supercell model with Fe-Fe bipyramids, Scaramucci *et al.* proceeded with the simulation of the chemical disorder within YBCFO and pointed out how  $B$ -site disorder affects the transition temperature  $T_{N2}$  [11].

Since both order parameters of magnetic and ferroelectric ordering are anisotropic, the study using a single crystal is therefore necessary. Using magnetization measurements on a high-quality single crystal of YBCFO, Lai *et al.* demonstrated that the magnetic moments of YBCFO lie on the  $ab$  plane and with a propagation vector along the  $c$  axis [12], which disagrees with the reported powder data and also explains the lack of ferroelectricity in a YBCFO single crystal [1,9]. The crystal structure of the YBCFO was also evidenced to possess a space group of  $P4/mmm$  by using x-ray multibeam resonant diffraction [13]. Furthermore, the Rietveld refinement revealed a collinear magnetic ordering type of  $\{+, -, -, +\}$  between  $T_{N1}$  and  $T_{N2}$ , which is a CM phase with propagation vector  $\mathbf{k}_{c1} = (1/2\ 1/2\ 1/2)$ . Once cooled to  $T_{N2}$ , two satellites of the ICM phase with  $\mathbf{k}_i = (1/2\ 1/2\ 1/2 \pm \delta)$  were observed from the separation of CM reflections, indicating the emergence of a helical magnetic structure.

Research about YBCFO is active because of its rich magnetic phase diagram and the potential for spintronic applications; however, puzzles remain: for example, the inconsistency of the CM-ICM transition temperature  $T_{N2}$  as reported for the powder samples. The  $T_{N2}$  has been reported to vary from 170 to 230 K [1,9,14]. Since the impurities of

the  $B$ -site ordering are essential to the magnetic behaviors of YBCFO, in this paper we carefully controlled the Cu/Fe ratio and the thermal treatments of polycrystalline samples of  $\text{YBa}(\text{Cu}_{1-x}\text{Fe}_x)_2\text{O}_5$  and then studied their susceptibility and magnetic structures by using magnetic susceptibility measurement, neutron- and x-ray powder diffractions (NPD and XRD).

## II. EXPERIMENTAL DETAILS

For this study, 13 polycrystalline samples of  $\text{YBa}(\text{Cu}_{1-x}\text{Fe}_x)_2\text{O}_5$ ,  $x = 0.465 \sim 0.535$ , were synthesized using the solid-state reaction method [15]. First, stoichiometric amounts of  $\text{Y}_2\text{O}_3$  (99.99%, ELECMAT),  $\text{BaCO}_3$  (99.9%, Tekstarter Co.),  $\text{CuO}$  (99.999%, Tekstarter Co.), and  $\text{Fe}_2\text{O}_3$  (above 99.99%, LTS Research Laboratories) were thoroughly mixed with a ceramic mortar and pestle before being placed into an alumina crucible. After being calcined at  $900^\circ\text{C}$  in air for 24 h, the black powders were fully ground and then sintered in air for 24 h. The sintering temperature,  $T_S$ , was adjusted between 1000 and  $1100^\circ\text{C}$  depending on the Cu/Fe ratio to eliminate possible impurities. The final mixtures were fully ground again before annealing at  $400^\circ\text{C}$  with  $\text{O}_2$  flow for another 24 h to compensate for oxygen deficiency. Every thermal treatment segment ended in a natural cooling process. All the samples were identified as a pure phase by utilizing an in-house x-ray powder diffractometer (Bruker D8 advance,  $\text{Cu}\ K_\alpha$ ). The magnetic property of the samples was first studied using a Magnetic Properties Measuring

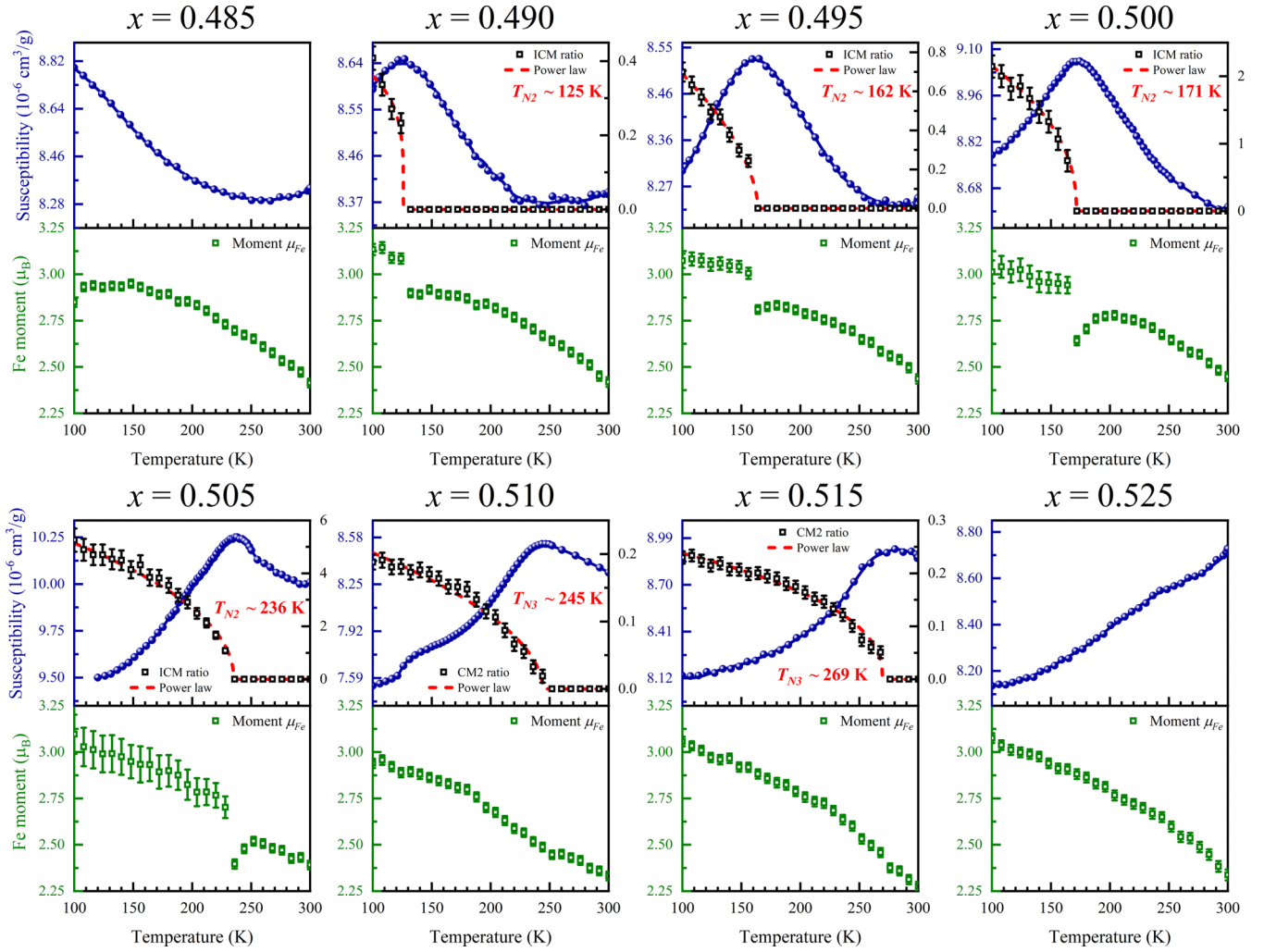


FIG. 2. In the same temperature range as Fig. 1, the temperature dependence of specific physical properties: The upper curves demonstrate the dc susceptibilities measured by heating after cooling in zero fields that overlapped by the ratio of ICM or CM2 phase (black squares) and their power-law fitting (red dashed line). The kinks of the susceptibility curves of  $x = 0.505$  and  $0.510$  are due to the change of warming rate during the magnetometry measurements, or due to the traced amount of  $\alpha$ - $\text{Fe}_2\text{O}_3$  and  $\text{Fe}_3\text{O}_4$  impurities below the detection limits of XRD and NPD experiment [21,22]. The lower insets (green squares) represent the magnetic moment of Fe, which is restricted to three times the Cu moments. During the refinement of the case of multiple magnetic phases, the magnetic moments in each magnetic phase are constrained to be identical. The obtained moment size needs to be multiplied by the factor  $\sqrt{(s_2 + s_3)/s_1}$  to consider the excessive magnetic phase volume, i.e.,  $(s_2 + s_3) > s_1$ . Here, the scale factor of the CM1 phase  $s_2$  is limited to the same as the nuclear scale  $s_1$ , and  $s_3$  is the scale factor of the ICM or CM2 phase.

System (Quantum Design) equipped with a highly sensitive superconducting quantum interference device.

The determination of the magnetic structures was carried out by using neutron powder diffraction on two diffractometers, Wombat and Echidna of ANSTO. Wombat is a high-flux neutron powder diffractometer and is suitable for rapid data collection [16]. For this study, neutrons were selected to be a wavelength of 2.95 Å by Ge (1 1 3) at a 120° take-off angle. Diffraction patterns of  $\text{YBa}(\text{Cu}_{1-x}\text{Fe}_x)_2\text{O}_5$  were collected from  $T = 100$  to 300 K with a step of 2 K. A more detailed study was performed on Echidna using neutrons with a wavelength of 2.4395 Å [selected by Ge (3 3 1)], which provides a higher spatial resolution [17]. The neutron-diffraction patterns were analyzed using the FULLPROF suite [18]. In our data refinement, since the Cu/Fe ions occupy two close sites, the diffractions that came from the Cu/Fe moments cannot be

determined, while some of the NPD patterns contain more than one magnetic propagation vector, indicating magnetic phase separation. Because the peak intensities are proportional to the scale factors and square of the magnetic moments, constraints of these parameters need to be made.

### III. RESULTS AND DISCUSSION

The XRD results of 13  $\text{YBa}(\text{Cu}_{1-x}\text{Fe}_x)_2\text{O}_5$  samples with different  $x$  indicate no impurity phases and all the samples are indexed with a space group  $P4/mmm$  (see Appendix A). The determination of the magnetic structural transition was conducted by using a high-flux neutron diffractometer of Wombat for 100 to 300 K. Figure 1 shows the contour plots summarizing the results taken from samples with  $x$  from 0.485 to 0.525. Except for the Bragg reflections from the host lat-

tice, these NPD patterns also show magnetic reflections with non-integer Millar indices. As shown in Fig. 1, for  $x = 0.500$ , magnetic reflections of the CM phase ( $1/2\ 1/2\ 1/2$ ) and ( $1/2\ 1/2\ 3/2$ ) split along  $Q$  at  $T_{N2} \sim 175$  K, which suggests a magnetic phase transition and is also consistent with the CM-ICM transition as observed for single crystal [12]. This CM-ICM transition is also observed for  $x = 0.490, 0.495, \text{ and } 0.505$ , but with different  $T_{N2}$ . When the Fe concentration reaches 0.510, a second commensurate magnetic phase, marked as CM2, appears at 245 K. This CM2 phase has a propagation vector  $\mathbf{k}_{c2} = (1/2\ 1/2\ 0)$ , which can also be observed for  $x = 0.515$  and 0.525. Overall, as shown in Fig. 1, the transition temperatures of the ICM or CM2 phase are sensitive to the Fe concentration, suggesting the important role played by the disorder strength at the  $B$  site for the variation of the magnetic structures [10,11]. The volume fraction of the magnetic phases and the moment of  $\text{Fe}^{3+}$  can be extracted, and both parameters combining the susceptibility data are displayed in Fig. 2.

The susceptibility provides unambiguous evidence for the magnetic phase transition of a material. As shown in Fig. 2, except for the two samples of  $x = 0.485$  and 0.525 that show no significant magnetic phase transition between 100 and 300 K, samples with  $x$  among 0.490 to 0.515 all show an AFM behavior as indicated with  $T_{N2}$  or  $T_{N3}$ , in addition to the  $T_{N1}$  in pristine YBCFO ( $x = 0.500$ ). These transitions agree with the NPD data. With the detailed magnetic structural information obtained from the high-resolution NPD data (as stated below), we carried out the refinements for the high-flux NPD data. The sample with  $x = 0.485$  shows only the initial commensurate phase, marked as CM1, while the sample with  $x = 0.525$  shows only the CM2 phase. As it warms up, each sample shows a different volume fraction of the ICM or CM2 in the crystal lattice, which is defined as the ratio of the magnetic phase scale factors,  $s3/s2$ , where  $s2$  is the scale factor of CM1 phase and  $s3$  is the scale factor of ICM or CM2 phase, as shown in Fig. 2. The scale factor is a linear parameter of the intensity formula applied in Rietveld refinement [18]. The ratios gradually decrease as temperature increases and can be fitted with a power law, indicating a second-order magnetic phase transition for ICM or CM2 phases. The best fits give rise to a transition temperature of  $T_{N2}$  or  $T_{N3}$  for each sample; for example, for the  $x = 0.490$  sample it undergoes a CM-ICM phase transition at  $T_{N2} = 125$  K and  $T_{N2} = 161$  K for  $x = 0.495$ . For the other magnetic phase CM2 appears at  $T_{N3} = 245$  K for  $x = 0.510$  while  $T_{N3} = 269$  K for  $x = 0.515$ .

The magnetic moment for each sample can be also extracted from the refinements. The plot of the magnetic moment of Fe as a function of temperature is shown in the open green squares (Fig. 2, lower panel). We limited the moments of Fe to three times the moments of Cu based on their effective magneton numbers [20], which can prevent the refinement from providing unreasonable results. The moment sizes of two coexisting phases are constrained to be the same since the moment size depends on the electron configuration structure and crystal-field environment. Meanwhile, to compensate for the difference in the scale factors between magnetic and nonmagnetic unit cells, the moment size has been corrected by multiplying the square root of the ratio between the sum of all scale factors of the magnetic phases

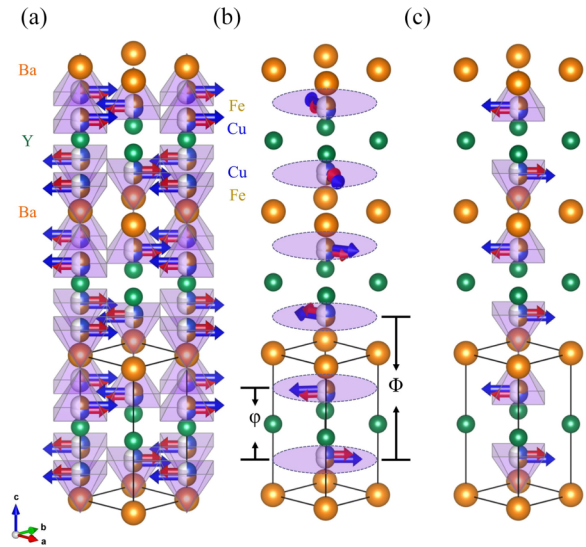


FIG. 3. Magnetic structures of (a) CM1 phase, (b) ICM phase, and (c) CM2 phase of  $\text{YBa}(\text{Cu}_{1-x}\text{Fe}_x)_2\text{O}_5$ . The moments of the closest Cu and Fe sites are constrained to the same direction, with a ratio of  $3\mu_{\text{Cu}} \approx \mu_{\text{Fe}}$  [20]. The scale of Cu moments is enhanced for easier inspection. Respectively, the phase angles of the ICM helix  $\varphi$  and  $\Phi$  associated with the satellite position and relative intensity between the two satellites [12]. For the same magnetic phase with a distinct  $x$ , there are only small divergences at the moment magnitude and phase angles (see Table I).

and the scale factor of the nuclear phase. The moment size should increase with cooling because of the lowering of thermal fluctuation. However, the corrected ICM moments show a discontinuous alteration while cooling down to  $T_{N2}$ , which is caused by forcing  $s3$  to 0 for  $T > T_{N2}$ .

In order to determine the magnetic structures as observed in the high-flux NPD patterns, high-resolution NPD patterns for all samples were measured at 1.5 K on the experimental station Echidna. The analyses of magnetic structures start with utilizing BasReps in the FULLPROF suite to complete the representation analysis. Based on the theorem first proposed by Bertaut [23], this process can provide possible magnetic structures from the symmetry-adapted basis vectors of each irreducible representation (*IRrep*). According to the candidates given by BasReps, the Rietveld refinement of  $\text{YBa}(\text{Cu}_{1-x}\text{Fe}_x)_2\text{O}_5$  high-resolution data was continued with FULLPROF. Eventually, the refinement result with *IRrep*(9) [analogous to the *IRrep*(10) of the CM1 phase; see Appendix D, Table IV] achieved satisfying goodness of fit that reveals the magnetic structure of the CM2 phase is a collinear magnetic ordering  $\{+, -, +, -\}$ , illustrated in Fig. 3(c), along with the collinear ordering  $\{+, -, -, +\}$  of CM1 and the helical ordering of ICM. To adapt all the bases of the *IRres*, the moments of two CM phases are limited to parallel the  $[1\ 1\ 0]$  direction. Nevertheless, refinements of the CM phases with any rotation along the  $c$  axis give comparable criteria of fit.

As shown in Fig. 4(a), magnetic reflections of CM1 ( $1/2\ 1/2\ 1/2$ ) and ( $1/2\ 1/2\ 3/2$ ), persist down to  $T = 1.5$  K for all seven samples, which agrees with reported NPD results [8–10]. The ICM phase characterized by reflections ( $1/2\ 1/2$

TABLE I. The Rietveld refinement results of the high-resolution data displayed in Fig. 5. Their transition temperatures  $T_{N2}$  and  $T_{N3}$  are indicated by the power-law fitting (see Fig. 2). The percentage of the second magnetic phase (ICM or CM2) is defined as  $s3/(s2 + s3)$ . The isotropic displacement  $B_{iso}$  of Cu and Fe is fixed to avoid unreasonable values ( $B_{iso} < 0$ ) given by FULLPROF and to reduce the number of fitting parameters. For the samples with coexisting magnetic phases, the error of magnetic moments is amplified after taking into account the error of the scales ( $s2$  and  $s3$ ). The difference in moment magnitude ascribed to the Cu/Fe ratio is trivial compared to the moment error. The low background and long counting time of the high-quality data restrict the criteria of fit  $R_{wp}$  and  $\chi^2$  to the less-satisfying values [24].

YBa(Cu <sub>1-x</sub> Fe <sub>x</sub> ) <sub>2</sub> O <sub>5</sub> at 1.5 K, SG: <i>P4/mmm</i>							
$x$	0.485	0.490	0.495	0.500	0.505	0.510	0.515
$T_S$ (°C)	1000	1000	1000	1000	1050	1100	1100
Phase transition	CM1	CM1	CM1	CM1	CM1	CM1	CM1
		↓	↓	↓	↓	↓	↓
		ICM	ICM	ICM	ICM	CM2	CM2
$T_{N2}$ or $T_{N3}$ (K)		125	161	171	236	245	269
ICM or CM2 percentage (%)	0	31(2)	54(2)	76(5)	85(7)	19(1)	22(1)
$a$ (Å)	3.8660(1)	3.8670(1)	3.8669(1)	3.8674(1)	3.8681(1)	3.8685(1)	3.8686(1)
$c$ (Å)	7.6409(1)	7.6417(1)	7.6389(1)	7.6363(1)	7.6341(1)	7.6362(1)	7.6356(1)
<b>Y (1b)</b>							
$B_{iso}$ (Å <sup>2</sup> )	0.646(46)	0.526(59)	0.411(42)	0.463(40)	0.337(43)	0.642(47)	0.413(43)
<b>Ba (1a)</b>							
$B_{iso}$ (Å <sup>2</sup> )	0.872(68)	0.609(87)	0.789(64)	0.885(62)	0.543(64)	0.806(70)	0.800(66)
<b>Cu (2h)</b>							
$z$	0.2833(6)	0.2814(10)	0.2807(7)	0.2830(6)	0.2804(8)	0.2840(7)	0.2829(7)
$B_{iso}$ (Å <sup>2</sup> )	0.101	0.101	0.101	0.101	0.101	0.101	0.101
$O_{cc}$	0.515	0.510	0.505	0.500	0.495	0.490	0.485
$\mu_{Cu}$ ( $\mu_B$ )	0.877(8)	1.023(65)	1.003(48)	1.028(94)	1.014(116)	0.957(36)	1.006(32)
<b>Fe (2h)</b>							
$z$	0.2554(6)	0.2583(9)	0.2581(6)	0.2568(5)	0.2586(7)	0.2559(5)	0.2568(5)
$B_{iso}$ (Å <sup>2</sup> )	0.101	0.101	0.101	0.101	0.101	0.101	0.101
$O_{cc}$	0.485	0.490	0.495	0.500	0.505	0.510	0.515
$\mu_{Fe}$ ( $\mu_B$ )	2.630(23)	3.070(196)	3.008(145)	3.084(281)	3.043(349)	2.871(107)	3.018(96)
<b>O1 (1c)</b>							
$B_{iso}$ (Å <sup>2</sup> )	0.472(39)	0.310(50)	0.268(35)	0.352(34)	0.162(36)	0.510(40)	0.307(36)
<b>O2 (4i)</b>							
$z$	0.3158(1)	0.3163(2)	0.3160(1)	0.3159(1)	0.3152(1)	0.3156(1)	0.3153(1)
$B_{iso}$ (Å <sup>2</sup> )	0.472(39)	0.310(50)	0.268(35)	0.352(34)	0.162(36)	0.510(40)	0.307(36)
$\varphi$ (°)	180	203(5)	186(2)	185(1)	188(1)	180	180
$\Phi$ (°)	180	149(1)	146(1)	147(1)	139(1)	0	0
$\chi^2$	6.97	9.11	5.49	7.48	6.88	12.2	8.78
$R_{wp}$ (%)	7.45	10.0	6.52	6.67	7.66	8.58	7.32
$R_{Bragg}$ (%)	2.70	3.30	2.19	2.32	2.77	2.90	3.05

$1/2 \pm \delta$ ) appears at the patterns with the Fe/Cu ratio  $0.490 \leq x \leq 0.505$ . For  $x = 0.510$  and  $0.515$ , extra reflections come out marked as CM2 characterized with a  $q$ -wave vector ( $1/2 \ 1/2 \ 0$ ), while the ICM phase is suppressed. Figures 4(b) and 4(c) exhibit the calculated patterns of  $x = 0.505$  and  $0.515$ . The structural parameters obtained from the Rietveld analysis are summarized in Table I. The variance in crystalline parameters is too subtle to intuitively interpret the emergence of this CM2 phase and the remarkable rise in the transition temperatures (see Appendix B). We use the *P4/mmm* model instead of the *P4mm* model to conduct the analysis because the agreement of fit does not benefit from its surplus degree of freedom. The refinement differences of the two models are discussed in Appendix C. Meanwhile, the spin ordering of the two commensurate phases cannot be intuitively derived from the representation analysis of *P4mm*, since the symmetry of the upper- and lower- $B$  sites is absent in this space group (see Appendix D).

As a comparison, a set of YBCFO ( $x = 0.500$ ) samples sintered at various temperatures without annealing was synthesized to examine how sintering temperature ( $T_S = 980, 1000, \text{ and } 1040^\circ \text{C}$ ) influenced  $T_{N2}$ . Their temperature dependence of magnetic susceptibility is shown in Figs. 5(a) to 5(c), demonstrating that the  $T_{N2}$  can be increased by increasing the sintering temperature. Once the sample was annealed at  $400^\circ \text{C}$  again, the  $T_{N2}$  was observed to decrease as well as shown in Fig. 5(d). This behavior can be understood to be due to the changes in disordering at the  $B$  sites by the different thermal synthesis processes [10].

In 2018, Scaramucci *et al.* developed a model to explain the cause of magnetic helix in YBaCuFeO<sub>5</sub> [11]. This model includes a superlattice with two times lattice parameter  $c$  and Cu-Fe bipyramids; this  $B$ -sites array along the  $c$ -axis, Cu-Cu-Fe-Fe, has been revealed as the lowest energy arrangement by *ab initio* calculations [9]. Regardless, as shown in Fig. 6, local impurity bonds Fe-O1-Fe, that connect two Fe and an

TABLE II. The Rietveld refinement details of the  $P4mm$  model, where the left data are the results from the  $P4/mmm$  model, and the lone values are constraints.

YBa(Cu <sub>1-x</sub> Fe <sub>x</sub> ) <sub>2</sub> O <sub>5</sub> at 1.5 K, SG: $P4mm$			
$x$	0.485	0.500	0.515
ICM or CM2 percentage (%)	0	76(5) → 86(6)	22(1) → 23(1)
$a$ (Å)	3.8660(1) → 3.8660(1)	3.8674(1) → 3.8674(1)	3.8686(1) → 3.8687(1)
$c$ (Å)	7.6409(1) → 7.6409(1)	7.6363(1) → 7.6363(1)	7.6356(1) → 7.6359(1)
<b>Y (1a)</b>			
$z$	0.5000 → 0.4980(11)	0.5000 → 0.5002(12)	0.5000 → 0.5016(13)
$B_{\text{iso}}$ (Å <sup>2</sup> )	0.646(46) → 0.523(56)	0.463(40) → 0.383(49)	0.413(43) → 0.377(52)
<b>Ba (1a)</b>			
$z$	0.0000	0.0000	0.0000
$B_{\text{iso}}$ (Å <sup>2</sup> )	0.872(68) → 0.560(76)	0.885(62) → 0.694(66)	0.800(66) → 0.544(76)
<b>Cu (1b)</b>			
$z$	0.2833(6) → 0.2848(8)	0.2830(6) → 0.2841(8)	0.2829(7) → 0.2835(9)
$B_{\text{iso}}$ (Å <sup>2</sup> )	0.101	0.101	0.101
$Occ$	0.515 → 0.721	0.500 → 0.700	0.485 → 0.679
$\mu_{\text{Cu}}$ ( $\mu_{\text{B}}$ )	0.877(8) → 0.870(7)	1.028(94) → 0.950(85)	1.006(32) → 0.708(23)
<b>Fe (1b)</b>			
$z$	0.2554(6) → 0.2545(7)	0.2568(5) → 0.2559(7)	0.2568(5) → 0.2560(7)
$B_{\text{iso}}$ (Å <sup>2</sup> )	0.101	0.101	0.101
$Occ$	0.485 → 0.291	0.500 → 0.300	0.515 → 0.309
$\mu_{\text{Fe}}$ ( $\mu_{\text{B}}$ )	2.630(23) → 2.609(22)	3.084(281) → 2.849(255)	3.018(96) → 2.125(70)
<b>O1 (1b)</b>			
$z$	0.0000 → -0.0039(13)	0.0000 → 0.0009(15)	0.0000 → -0.0025(14)
$B_{\text{iso}}$ (Å <sup>2</sup> )	0.472(39) → 0.382(43)	0.352(34) → 0.300(37)	0.307(36) → 0.187(42)
<b>O2 (2c)</b>			
$z$	0.3158(1) → 0.3335(19)	0.3159(1) → 0.3334(18)	0.3153(1) → 0.3310(25)
$B_{\text{iso}}$ (Å <sup>2</sup> )	0.472(39) → 0.382(43)	0.352(34) → 0.300(37)	0.307(36) → 0.187(42)
<b>O2' (2c)</b>			
$z$	0.6842(1) → 0.7013(18)	0.6841(1) → 0.7012(17)	0.6847(1) → 0.7003(24)
$B_{\text{iso}}$ (Å <sup>2</sup> )	0.472(39) → 0.382(43)	0.352(34) → 0.300(37)	0.307(36) → 0.187(42)
$\varphi$ (°)	180	185(1) → 187(1)	180
$\Phi$ (°)	180	147(1) → 146(1)	0
$\chi^2$	6.97 → 6.91	7.48 → 7.27	8.78 → 9.14
$R_{\text{B}1}$ (%)	2.70 → 2.50	2.32 → 2.12	3.05 → 2.90
$R_{\text{B}2}$ (%)	17.3 → 17.5	16.5 → 16.2	17.5 → 16.5
$R_{\text{B}3}$ (%)	—	13.1 → 12.8	19.3 → 24.5

apical O1 of a bipyramid, are randomly inserted into the Cu-Fe bipyramids of this model. These impurities occupy only a few percent of all Cu-Fe bipyramids, while the same amounts of Cu–O1–Cu impurity bonds are generated to balance the stoichiometry [11]. The concentration of impurity bonds (Fe–Fe bipyramids) defines the chemical disorder of a sample, which is the most crucial variable of the magnetic properties of YBaCuFeO<sub>5</sub>. The spin orderings of YBaCuFeO<sub>5</sub> were interpreted by introducing Heisenberg Hamiltonians: the exchange interaction among  $B$  sites combines two Cu-Fe bipyramids that are divided by the Y layer is AFM, and the superexchange formed of an apical O1 and  $B$  sites of the Cu-Fe bipyramids is ferromagnetic (FM). The superexchange induced by the impurity bonds belongs to this coupling too, while the superexchange in the  $ab$  plane formed of a basal O2 and  $B$  sites of the Cu-Fe bipyramids is AFM. These three couplings construct the magnetic structure of CM1 with  $\mathbf{k}_{c1} = (1/2 \ 1/2 \ 1/2)$ . As illustrated in Fig. 6(a), the ordering of the middle superlattice is  $\{+, -, -, +\}$  surrounded by the four nearest lattices in the  $ab$  plane, whose ordering is

$\{-, +, +, -\}$ . After cooling down below  $T_{N2}$  or  $T_{N3}$ , the coupling contributed by the impurity bonds will transform into an AFM coupling much stronger than other couplings along the  $c$  axis. In this case, the ordering of the superlattice with an impurity bond should be  $\{+, -, +, -\}$  so it can have the lowest energy. Yet, by assuming no Fe-Fe bipyramids joined aside (the in-plane minimum distance is larger than lattice parameter  $a$ ; see Ref. [11]) and because of the in-plane AFM coupling, the surrounded  $\{-, +, +, -\}$  orderings do not accept this spin reorientation and then the competition begins. Due to an even match between the AFM couplings, this chemical disorder brings about a local spin frustration and leads to the ICM spin helix demonstrated in Fig. 6(b). On the other hand, if the chemical disorder is increased to some extent the strong AFM coupling could dominate the whole system and further create the spin ordering  $\{+, -, +, -\}$  as exhibited in the middle superlattice in Fig. 6(c). By substituting more Fe into  $B$  sites, the possibility of possessing the Fe-Fe bipyramids is magnified; hence, it is reasonable that the YBCFO sample with higher  $x$  has a higher chemical

TABLE III. The Rietveld refinement details of the canted magnetic structures, again the lone values are constraints.

YBa(Cu <sub>1-x</sub> Fe <sub>x</sub> ) <sub>2</sub> O <sub>5</sub> at 1.5 K, SG: <i>P4/mmm</i>		
<i>x</i>	0.500	0.510
ICM or CM2 percentage (%)	76(5) → 75(5)	19(1) → 20(1)
<i>a</i> (Å)	3.8674(1) → 3.8674(1)	3.8685(1) → 3.8685(1)
<i>c</i> (Å)	7.6363(1) → 7.6362(1)	7.6362(1) → 7.6363(1)
<b>Y (1b)</b>		
<i>B</i> <sub>iso</sub> (Å <sup>2</sup> )	0.463(40) → 0.490(39)	0.642(47) → 0.583(44)
<b>Ba (1a)</b>		
<i>B</i> <sub>iso</sub> (Å <sup>2</sup> )	0.885(62) → 0.880(60)	0.806(70) → 0.746(66)
<b>Cu (2h)</b>		
<i>z</i>	0.2830(6) → 0.2830(6)	0.2840(7) → 0.2827(7)
<i>B</i> <sub>iso</sub> (Å <sup>2</sup> )	0.101	0.101
<i>Occ</i>	0.500	0.490
$\mu_{\text{Cu}}$ ( $\mu_{\text{B}}$ )	1.028(94) → 0.979(82)	0.957(36) → 0.947(33)
<b>Fe (2h)</b>		
<i>z</i>	0.2568(5) → 0.2568(5)	0.2559(5) → 0.2571(6)
<i>B</i> <sub>iso</sub> (Å <sup>2</sup> )	0.101	0.101
<i>Occ</i>	0.500	0.510
$\mu_{\text{Fe}}$ ( $\mu_{\text{B}}$ )	3.084(281) → 2.936(246)	2.871(107) → 2.840(99)
<b>O1 (1c)</b>		
<i>B</i> <sub>iso</sub> (Å <sup>2</sup> )	0.352(34) → 0.372(34)	0.510(40) → 0.415(38)
<b>O2 (4i)</b>		
<i>z</i>	0.3159(1) → 0.3159(1)	0.3153(1) → 0.3156(1)
<i>B</i> <sub>iso</sub> (Å <sup>2</sup> )	0.352(34) → 0.372(34)	0.510(40) → 0.415(38)
$\theta$ (°)	90 → 45	90 → 50
$\varphi$ (°)	185(1) → 185(1)	180
$\Phi$ (°)	147(1) → 146(1)	0
$\chi^2$	7.48 → 7.17	12.2 → 11.1
<i>R</i> <sub>B1</sub> (%)	2.32 → 2.47	2.90 → 2.79
<i>R</i> <sub>B2</sub> (%)	16.5 → 11.8	19.5 → 15.6
<i>R</i> <sub>B3</sub> (%)	13.1 → 12.0	31.7 → 27.5

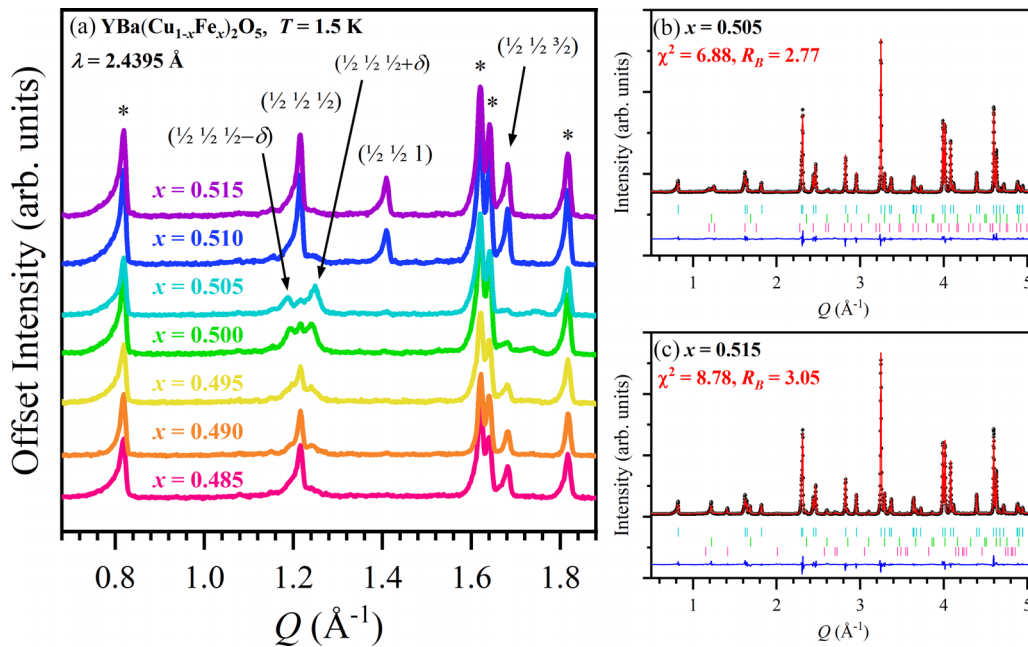


FIG. 4. The high-resolution NPD patterns of  $x = 0.485$  to  $x = 0.515$ . (a) Comparison for all samples. The four Bragg peaks labeled with \* are (0 0 1), (1 0 0), (0 0 2), and (1 0 1) along the  $Q$  direction. (b), (c) Refinement results of (b)  $x = 0.505$  and (c)  $x = 0.515$ . Black dots: observed data. Red curves: calculated data. Blue curves: the difference between refinement and experiment. Bars mark out the peak positions of each phase. Their refined parameters are listed in Table I.

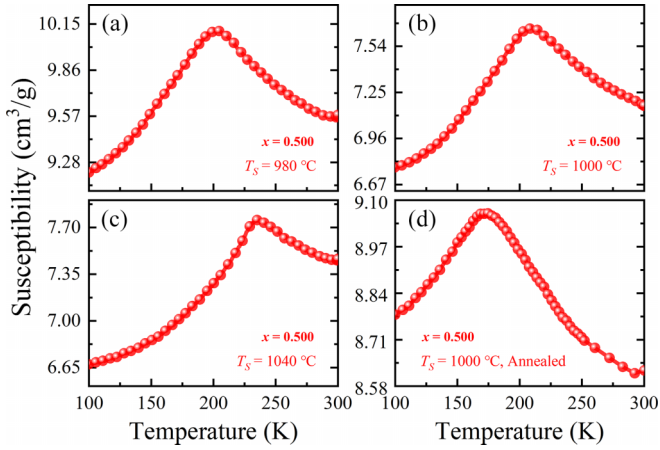


FIG. 5. The dc magnetic susceptibilities of  $\text{YBaCuFeO}_5$  ( $x = 0.500$ ) experienced distinct thermal treatments that were measured by heating after cooling in zero fields. (a)–(c) Samples were sintered at  $T_S = 980, 1000,$  and  $1040^\circ\text{C}$  without annealing. (d) Similar to (b), the sample was sintered at  $T_S = 1000^\circ\text{C}$  and then annealed at  $400^\circ\text{C}$ .

disorder, and those samples with  $x \geq 0.510$  demonstrate the CM2 phase instead of the ICM phase, where the magnetic structure of CM2 with  $\mathbf{k}_{c2} = (1/2 \ 1/2 \ 0)$  is exactly the same as in Fig. 6(c).

This model can also clarify why CM1 lasts even at 1.5 K. The influence of the  $B$ -site disorder needs the bonds parallel to the  $ab$  plane as media to propagate, but these bonds break on the edge of powder particles. Countless powder particles share a small number of Fe impurities in a portion of powder sample (up to 10 grams for NPD measurements), so there must be many powder particles without any  $B$ -site impurities that still prefer the CM1 spin ordering after cooling down below  $T_{N2}$  or  $T_{N3}$ . The Monte Carlo simulation results of Scaramucci *et al.* suggested  $T_{N2}$  could be raised with higher chemical disorder [11]. This agrees with our result of  $T_{N2}$  (see Table I) that samples with higher  $x$  indicate higher  $T_{N2}$  and the same phenomenon also reflects in the connection between  $T_{N3}$  and  $x$ . The magnetic susceptibility data also indicate the transition temperature  $T_{N2}$  can be modified by various thermal treatments. Considering the complexity of states of chemical disorder, the free-energy potential of  $\text{YBaCuFeO}_5$  contains multiple local minima at distinct degrees of chemical disorder, while the real ground state sits on a fully ordered state as Morin *et al.* proposed [9]. When a  $\text{YBaCuFeO}_5$  sample is naturally cooled after the sintering process, its free energy will drop toward zero and eventually sink into one of the local minima with a nonzero chemical disorder. By sintering the sample at a higher temperature, the provided energy may excite it to a state of more chemical disorder, so the final state could have more  $B$ -site impurities under a similar cooling time. Meanwhile, annealing a sample could irrigate sufficient energy for it to escape from the local minimum and then drop to another metastable state with more ordered  $B$  sites. Morin *et al.* tested various cooling conditions on  $\text{YBaCuFeO}_5$  and pointed out the quenched sample reveals much higher  $T_{N2}$  than the slow-cooled sample [10]. Analogously, a quenching treatment will freeze the sample to the metastable state close to the highest chemical disorder that the sintering temperature can

ever reach; on the contrary, slow cooling supplies the sample enough time and thermal energy to travel through more local minimum valleys before getting fully steady. However, the CM2 phase cannot be generated with such methods, no matter how many Fe-Fe bipyramids these  $\text{YBaCuFeO}_5$  samples possess. The chemical disorder originating from Fe substitution in general is different from thermal treatments since it not only produces Fe impurities but also annihilates Cu impurity bonds at the same time.

#### IV. CONCLUSIONS

In summary, we demonstrate a tunable magnetic phase transition in the helimagnet  $\text{YBa}(\text{Cu}_{1-x}\text{Fe}_x)_2\text{O}_5$  by tuning the Cu/Fe ratio. This change not only largely increases the transition temperature for the spiral magnetic phase from  $T = 125$  to  $269$  K, for  $0.490 \leq x \leq 0.505$ , but also induces a commensurate phase CM2 with a collinear AFM ordering for  $x \geq 0.510$ . The phase diagram of  $\text{YBa}(\text{Cu}_{1-x}\text{Fe}_x)_2\text{O}_5$  is illustrated in Fig. 7. In addition, we also demonstrate that the enhancement of the transition temperature  $T_{N2}$  can also be done with different thermal treatments, which is to induce randomness disorders like the chemical disorder by doping. This rich and complex phase diagram can be understood within the framework of randomness disorders around the Fe-O and Cu-O environments. Materials possessing a spiral spin ordering can be good candidates for showing magnetoelectricity effect and be potentially useful for spintronics [25–27], particularly with a transition temperature close to room temperature. In order to further understand the correlation of magnetoelectric coupling and chemical disorder in  $\text{YBa}(\text{Cu}_{1-x}\text{Fe}_x)_2\text{O}_5$ , investigations with high-quality single crystals are required and in progress.

#### ACKNOWLEDGMENTS

This work is funded by NSTC of Taiwan through Grants No. 112–2112-M-032–025 and No. 112–2623-E-032–001-NU. The authors are grateful to NSRRC for providing the travel grant to carry out neutron experiments at ANSTO and also thank NSRRC and ANSTO for the arrangements of the experimental beamtimes. W.-T.C. would like to acknowledge NSTC, Taiwan, for funding Grants No. 111–2112-M-002–044-MY3 and No. 112–2124-M-002–012, and Academia Sinica Project No. AS-iMATE-113–12.

#### APPENDIX A: IN-HOUSE XRD CHARACTERIZATION

Figure 8, a 2D contour, shows the XRD results of 13  $\text{YBa}(\text{Cu}_{1-x}\text{Fe}_x)_2\text{O}_5$  samples with different  $x$ . The differences in the lattice parameters for each sample are indistinguishable within the current resolution (the small variations of lattices are listed in Table I). The clear strips parallel to the  $x$  axis imply that the symmetry of the samples does not change by Cu/Fe ratio.

#### APPENDIX B: CRYSTALLINE INFORMATION

Figure 9(a) displays that bond-valence sums of individual sites and lattice parameters hardly changed from  $x = 0.485$  to  $0.515$ . On the other hand, Figs. 9(c) and 9(d) expose how



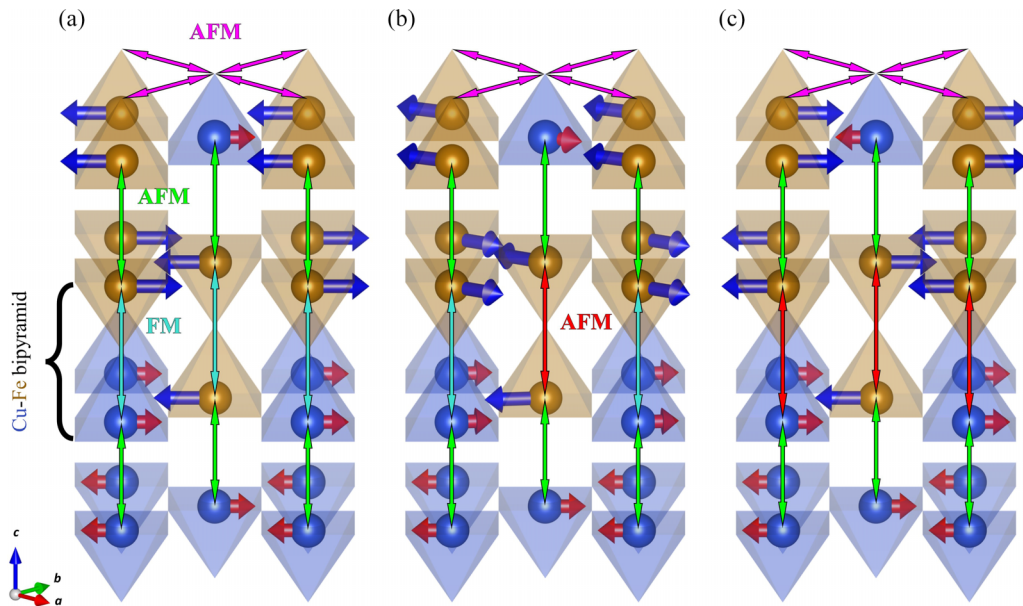


FIG. 6. The YBCFO superlattices are constructed from *B*-site pyramids with magnetic orderings of (a) CM1 phase, (b) ICM phase, and (c) CM2 phase. The turquoise double arrows represent the FM exchange coupling within the Cu-Fe bipyramids, while other double arrows stand for three different AFM interactions. The magnitudes of these exchange couplings have the following relations:  $|J_{c, \text{red}}| \gg |J_{ab, \text{magenta}}| \gg |J_{c, \text{green}}| > |J_{c, \text{turquoise}}|$  [11]. The local spin frustration is induced by the bipyramid consisting of only Fe *B* sites. The phase transition from (a) to (b) happens at  $T_{N2}$ , in other words, replacing the turquoise coupling of the Fe-Fe bipyramid with the red coupling should flip the middle Fe moment  $180^\circ$  parallel to the other four Fe moments in the same layer, but these Fe neighbors do not appreciate the alteration due to the magenta double arrows are AFM interactions. Instead, they rotate in the *ab* plane to keep opposite against the middle Fe moment, and this spin frustration propagates along the *c* axis to the entire system and then creates a helical spin ordering. If the number of the red coupling is enough to compress all the influence of the FM couplings, as shown in (c), it will be analogous to that all exchange interactions are AFM.

Fe concentration affects the bond lengths and angles that are pointed out by the inset (b). Here, O1 and O2 are located at the apical and the basal of the pyramid, respectively. The steadiness of the bond angle Cu–O1–O2 and the oxygen bonds O1–O2 and O2–O2 implies the shape and size of the double pyramids are fixed, and similar to the lattice are independent of *x*. By examining the curves of the bonds that connect O1 to the *B* sites, we understand that the Cu and the Fe ions in the same pyramid move in the opposite direction along the *c* axis to adapt to different Cu/Fe ratios, while the relations among *x* and other bond parameters covered in Fig. 9(d) are just the

geometrically inevitable response to this circumstance inside a limited pyramid.

### APPENDIX C: ANALOGIES WITH OTHER REFINED MODELS

In order to clear the disagreements between our refinements and reported models, we finished the refinements with those models and compared the results. First, some

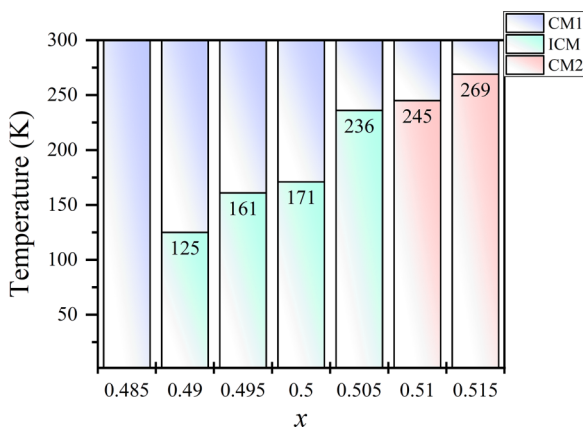


FIG. 7. The phase diagram of YBa(Cu<sub>1-x</sub>Fe<sub>x</sub>)<sub>2</sub>O<sub>5</sub>.

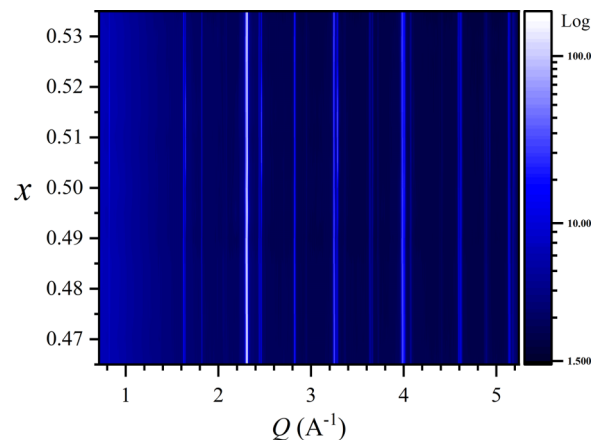


FIG. 8. Two-dimensional contour constructed of XRD patterns between  $2\theta$  equals  $10^\circ$  to  $80^\circ$  measured at room temperature; the 13 YBa(Cu<sub>1-x</sub>Fe<sub>x</sub>)<sub>2</sub>O<sub>5</sub> samples are  $x = 0.465, 0.470, 0.475, 0.485, 0.490, 0.495, 0.500, 0.505, 0.510, 0.515, 0.525, 0.530, \text{ and } 0.535$ .

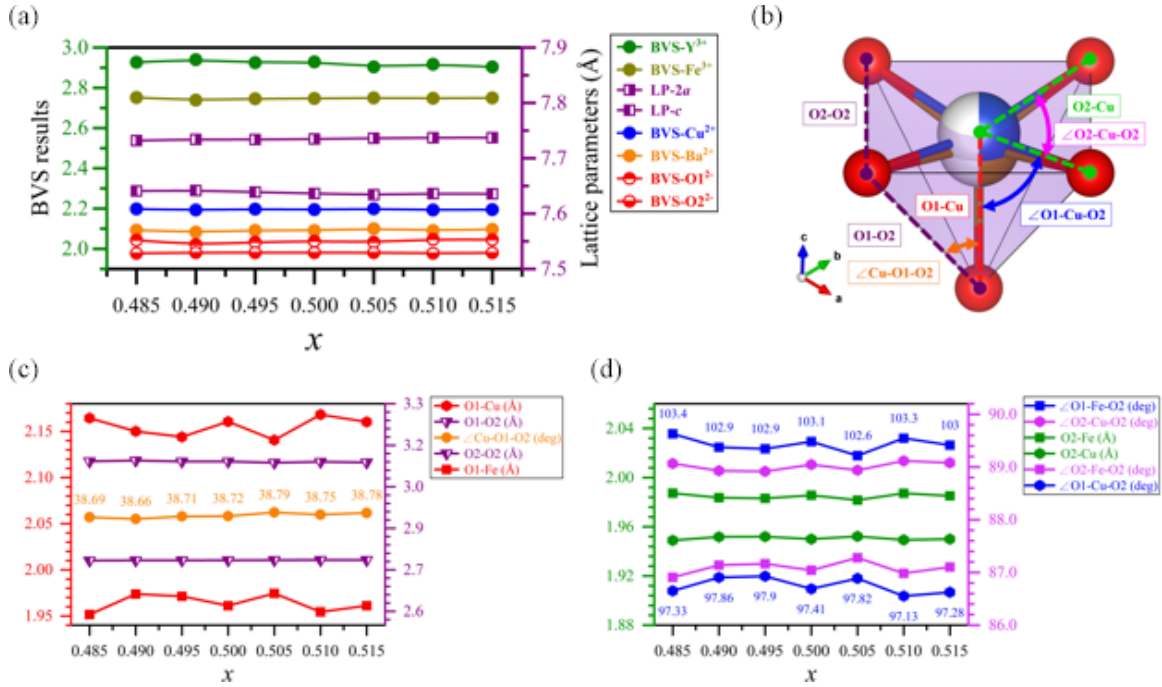


FIG. 9. (a) Bond-valence sums and lattice parameters of  $\text{YBa}(\text{Cu}_{1-x}\text{Fe}_x)_2\text{O}_5$  extracted from the Rietveld refinements. The bond-valence sums were calculated by referring to the parameters suggested by Brown and Altermatt [28]. (c), (d) Fe concentration dependence of bond lengths and angles specified in the inset (b). Notice the variables involving Fe are denoted as squares, while the variables attached to Cu are denoted as hexagons. Within a pyramid of constant size and shape, a longer O1–Cu bond is definitely accompanied by shorter O2–Cu bonds and generates an analogous tendency for bond angles.

researchers declared  $\text{YBaCuFeO}_5$  belongs to space group  $P4mm$ , instead of  $P4/mmm$  [9,10]. By removing a mirror plane perpendicular to the  $c$  axis, space group  $P4mm$  not only provides more degrees of freedom for atomic positions but also allows the upper and lower pyramids occupied by asymmetry amounts of Cu and Fe. The refinement results of  $x = 0.485, 0.500$ , and  $0.515$  with space group  $P4mm$  are listed in Table II. They show similar agreements of fit to the analyses with the  $P4/mmm$  model. The space group of  $\text{YBaCuFeO}_5$  was also confirmed to be  $P4/mmm$  with the use of x-ray multibeam resonant diffraction on a single crystal of  $\text{YBaCuFeO}_5$  [13]. The most obvious diversity between these two models is the ratio of the ICM phase. Since Cu and Fe have comparable neutron-scattering lengths, it is impossible to identify these models with nuclear-scattering data. However, the Fe moments are three times larger than the Cu moments, so the scale of the ICM phase must be increased to compensate for the loss of the magnetic structure factor caused by trading an Fe ion of the lower pyramid for a Cu ion from the upper pyramid. The other parameter we have not used is the canted angle between the magnetic moments and the  $c$  axis. Reported results indicate this angle  $\theta$  equals  $45^\circ$  at 1.5 K [9]. The refinement results of  $x = 0.500$  and  $0.510$  with this extra degree of freedom are listed in Table III, and Fig. 10 illustrates their magnetic structures. The criteria of fit of individual magnetic phases are improved by up to 4.7% with this canted angle. Nevertheless, there are two reasons we do not prefer these models; first, the magnetic susceptibility measurements of the YBCFO single crystal already indicated its easy plane is the  $ab$  plane, so the canted angle  $\theta$  must be a right angle to obey

the single-crystal results [12], and there is no evidence that Fe substitution can tilt magnetic moments toward the  $c$  axis. Meanwhile, when it comes to group theory, most theorists will refer to the Landau theory, which states that for a second-order

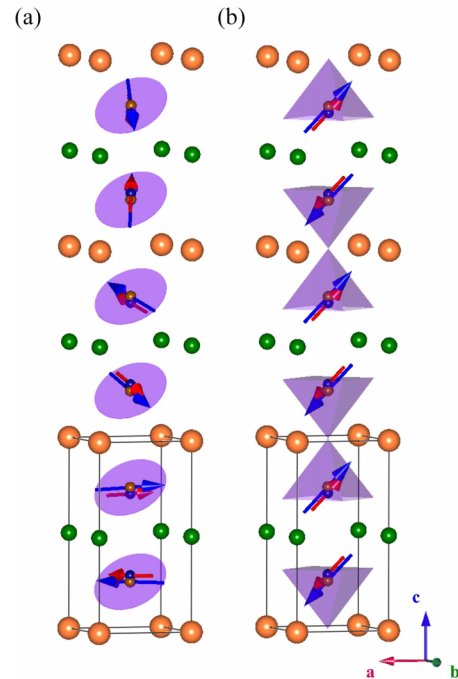


FIG. 10. The magnetic structures of (a) canted spin helix of ICM phase, and (b) canted collinear AFM of CM2 phase.

phase transition, the magnetic structure can only involve the basis vectors that belong to a single  $IRrep$  [29]. In order to

add the extra moments along the  $c$  axis, another basis from a second  $IRrep$  must be included (see Appendix D).

#### APPENDIX D: REPRESENTATION ANALYSIS RESULTS GIVEN BY BASIREPS

Table IV lists the representation analysis calculated with BasIREps. The basis vectors of the spin ordering could vary with the propagation vector and the Wyckoff positions.

TABLE IV. The representation analyses given by BasIREps: the left column is calculated based on the space group  $P4/mmm$  and the right column is based on  $P4mm$ .

Magnetic phase	Commensurate phase I (CM1)	
Propagation vector	$k_{c1} = (1/2 \ 1/2 \ 1/2)$	
Space group	$P4/mmm$	$P4mm$
Wyckoff positions	<b>2h</b> : $(1/2, 1/2, z), (1/2, 1/2, -z)$	<b>1b</b> : $(1/2, 1/2, z)$
$IRrep$	$IRrep(3)$	$IRrep(3)$
Basis vectors	$(x, y, z): [0, 0, [1]]$ $(-x + 1, y, -z + 1): [0, 0, -1]$	$(x, y, z): [0, 0, [1]]$
$IRrep$	$IRrep(6)$	$IRrep(5)$
Basis vectors	$(x, y, z): [0, 0, [1]]$ $(-x + 1, y, -z + 1): [0, 0, [1]]$	$(x, y, z): [1, i, 0] [1, -i, 0]$
$IRrep$	$IRrep(9)$	
Basis vectors	$(x, y, z): [0, 1, 0] [-1, 0, 0]$ $(-x + 1, y, -z + 1): [0, 1, 0] [-1, 0, 0]$	
$IRrep$	$IRrep(10)$	
Basis vectors	$(x, y, z): [1, 0, 0] [0, 1, 0]$ $(-x + 1, y, -z + 1): [-1, 0, 0] [0, -1, 0]$	
Magnetic phase	Incommensurate phase (ICM)	
Propagation vector	$k_i = (1/2 \ 1/2 \ 1/2 \pm \delta)$	
Space group	$P4/mmm$	$P4mm$
Wyckoff positions	<b>2h</b> : $(1/2, 1/2, z), (1/2, 1/2, -z)$	<b>1b</b> : $(1/2, 1/2, z),$
$IRrep$	$IRrep(3)$	$IRrep(3)$
Basis vectors	$(x, y, z): [0, 0, [1]]$	$(x, y, z): [0, 0, [1]]$
$IRrep$	$IRrep(5)$	$IRrep(5)$
Basis vectors	$(x, y, z): [1, i, 0] [1, -i, 0]$	$(x, y, z): [1, i, 0] [1, -i, 0]$
Magnetic phase	Commensurate phase II (CM2)	
Propagation vector	$k_{c2} = (1/2, 1/2, 0)$	
Space group	$P4/mmm$	$P4mm$
Wyckoff positions	<b>2h</b> : $(1/2, 1/2, z), (1/2, 1/2, -z)$	<b>1b</b> : $(1/2, 1/2, z)$
$IRrep$	$IRrep(3)$	$IRrep(3)$
Basis vectors	$(x, y, z): [0, 0, [1]]$ $(-x + 1, y, -z + 1): [0, 0, [1]]$	$(x, y, z): [0, 0, [1]]$
$IRrep$	$IRrep(6)$	$IRrep(5)$
Basis vectors	$(x, y, z): [0, 0, [1]]$ $(-x + 1, y, -z + 1): [0, 0, -1]$	$(x, y, z): [1, i, 0] [1, -i, 0]$
$IRrep$	$IRrep(9)$	
Basis vectors	$(x, y, z): [0, 1, 0] [-1, 0, 0]$ $(-x + 1, y, -z + 1): [0, -1, 0] [1, 0, 0]$	
$IRrep$	$IRrep(10)$	
Basis vectors	$(x, y, z): [1, 0, 0] [0, 1, 0]$ $(-x + 1, y, -z + 1): [1, 0, 0] [0, 1, 0]$	

[1] B. Kundys, A. Maignan, and C. Simon, Multiferroicity with high- $T_C$  in ceramics of the ordered perovskite  $YBaCuFeO_5$ , *Appl. Phys. Lett.* **94**, 072506 (2009).

[2] D. Khomskii, Classifying multiferroics: Mechanisms and effects, *phys.* **2**, 20 (2009).

[3] M. M. Vopson, Fundamentals of multiferroic materials and their possible applications, *Crit. Rev. Solid State Mater. Sci.* **40**, 223 (2015).

[4] A. Urushibara, Y. Moritomo, T. Arima, A. Asamitsu, G. Kido, and Y. Tokura, Insulator-metal transition and giant

- magnetoresistance in  $\text{La}_{1-x}\text{Sr}_x\text{MnO}_3$ , *Phys. Rev. B* **51**, 14103 (1995).
- [5] L. Chen, C. Yuan, J. Xue, and J. Wang, B-site ordering and magnetic behaviours in Ni-doped double perovskite  $\text{Sr}_2\text{FeMoO}_6$ , *J. Phys. D: Appl. Phys.* **38**, 4003 (2005).
- [6] Y.-jia Bai, Y.-jie Xia, H.-ping Li, L. Han, Z.-chang Wang, X.-jie Wu, S.-hui Lv, X.-juan Liu, and J. Meng, A-site-doping enhanced B-site ordering and correlated magnetic property in  $\text{La}_{2-x}\text{Bi}_x\text{CoMnO}_6$ , *J. Phys. Chem. C* **116**, 16841 (2012).
- [7] T. Shang, E. Canévet, M. Morin, D. Sheptyakov, M. T. Fernández-Díaz, E. Pomjakushina, and M. Medarde, Design of magnetic spirals in layered perovskites: Extending the stability range far beyond room temperature, *Sci. Adv.* **4**, eaau6386 (2018).
- [8] X.-dong Zhang, A. Romaguera, F. Sandiumenge, O. Fabelo, J. Blasco, J. Herrero-Martín, and J. L. García-Muñoz, Magnetic properties of a highly ordered single crystal of the layered perovskite  $\text{YBaCuFe}_{0.95}\text{Mn}_{0.05}\text{O}_5$ , *J. Magn. Magn. Mater.* **551**, 169165 (2022).
- [9] M. Morin, A. Scaramucci, M. Bartkowiak, E. Pomjakushina, G. Deng, D. Sheptyakov, L. Keller, J. Rodríguez-Carvajal, N. A. Spaldin, M. Kenzelmann *et al.*, Incommensurate magnetic structure, Fe/Cu chemical disorder, and magnetic interactions in the high-temperature multiferroic  $\text{YBaCuFeO}_5$ , *Phys. Rev. B* **91**, 064408 (2015).
- [10] M. Morin, E. Canévet, A. Raynaud, M. Bartkowiak, D. Sheptyakov, B. Voraksmy, M. Kenzelmann, E. Pomjakushina, K. Conder, and M. Medarde, Tuning magnetic spirals beyond room temperature with chemical disorder, *Nat. Commun.* **7**, 13758 (2016).
- [11] A. Scaramucci, H. Shinaoka, M. V. Mostovoy, M. Müller, C. Mudry, M. Troyer, and N. A. Spaldin, Multiferroic magnetic spirals induced by random magnetic exchanges, *Phys. Rev. X* **8**, 011005 (2018).
- [12] Y.-C. Lai, C.-H. Du, C.-H. Lai, Y.-H. Liang, C.-W. Wang, K. C. Rule, H.-C. Wu, H.-D. Yang, W.-T. Chen, G.-J. Shu *et al.*, Magnetic ordering and dielectric relaxation in the double perovskite  $\text{YBaCuFeO}_5$ , *J. Phys.: Condens. Matter* **29**, 145801 (2017).
- [13] W.-C. Liu, Y.-Z. Zheng, Y.-C. Chih, Y.-C. Lai, Y.-W. Tsai, Y.-Z. Zheng, C.-H. Du, F.-C. Chou, Y.-L. Soo, and S.-L. Chang, X-ray multi-beam resonant diffraction analysis of crystal symmetry for layered perovskite  $\text{YBaCuFeO}_5$ , *J. Appl. Crystallogr.* **49**, 1721 (2016).
- [14] Y. Kawamura, T. Kai, E. Satomi, Y. Yasui, Y. Kobayashi, M. Sato, and K. Kakurai, High-temperature multiferroic state of  $\text{RBaCuFeO}_5$  ( $R = \text{Y, Lu, and Tm}$ ), *J. Phys. Soc. Jpn* **79**, 073705 (2010).
- [15] L. Er-Rakho, C. Michel, P. Lacorre, and B. Raveau,  $\text{YBaCuFeO}_{5+\delta}$ : A novel oxygen-deficient perovskite with a layer structure, *J. Solid State Chem.* **73**, 531 (1988).
- [16] A. J. Studer, M. E. Hagen, and T. J. Noakes, Wombat: The high-intensity powder diffractometer at the OPAL reactor, *Physica B* **385**, 1013 (2006).
- [17] M. Avdeev and J. R. Hester, ECHIDNA: A decade of high-resolution neutron powder diffraction at OPAL, *J. Appl. Crystallogr.* **51**, 1597 (2018).
- [18] J. Rodríguez-Carvajal, Recent advances in magnetic structure determination by neutron powder diffraction, *Physica B* **192**, 55 (1993).
- [19] D. S. Sivia, *Elementary Scattering Theory: For X-ray and Neutron Users* (Oxford University Press, New York, NY, 2011).
- [20] C. Kittel, *Introduction to Solid State Physics*, 8th ed. (John Wiley & Sons, Hoboken, NJ, 2004).
- [21] S. Mitra, S. Das, S. Basu, P. Sahu, and K. Mandal, Shape- and field-dependent Morin transitions in structured  $\alpha\text{-Fe}_2\text{O}_3$ , *J. Magn. Magn. Mater.* **321**, 2925 (2009).
- [22] K. B. Paul, Magnetic and transport properties of monocrytalline  $\text{Fe}_3\text{O}_4$ , *Open Phys.* **3**, 115 (2005).
- [23] E. F. Bertaut, Representation analysis of magnetic structures, *Acta Crystallogr. A* **24**, 217 (1968).
- [24] B. H. Toby, R factors in Rietveld analysis: How good is good enough? *Powder Diffr.* **21**, 67 (2006).
- [25] T. Kimura, Spiral magnets as magnetoelectrics, *Annu. Rev. Mater. Res.* **37**, 384 (2007).
- [26] D. Kurebayashi and N. Nagaosa, Electromagnetic response in spiral magnets and emergent inductance, *Commun. Phys.* **4**, 260 (2021).
- [27] V. Baltz, A. Manchon, M. Tsoi, T. Moriyama, T. Ono, and Y. Tserkovnyak, Antiferromagnetic spintronics, *Rev. Mod. Phys.* **90**, 015005 (2018).
- [28] I. D. Brown and D. Altermatt, Bond-valence parameters obtained from a systematic analysis of the inorganic crystal structure database, *Acta Crystallogr. B* **41**, 244 (1985).
- [29] A. Willis, Magnetic structures and their determination using group theory, *J. Phys. IV France* **11**, Pr9 (2001).